PHYSICAL REVIEW E **69**, 051607 (2004)

Phase-field modeling of binary alloy solidification with coupled heat and solute diffusion

J. C. Ramirez,[1] C. Beckermann,[1,*] A. Karma,[2] and H.-J. Diepers[2,3]
[1]*Department of Mechanical and Industrial Engineering, The University of Iowa, Iowa City, Iowa 52242, USA*
[2]*Department of Physics and Center for Interdisciplinary Research on Complex Systems, Northeastern University, Boston, Massachusetts 02115, USA*
[3]*ACCESS e.V., D-52056 Aachen, Germany*

(Received 9 December 2003; published 28 May 2004)

A phase-field model is developed for simulating quantitatively microstructural pattern formation in solidification of dilute binary alloys with coupled heat and solute diffusion. The model reduces to the sharp-interface equations in a computationally tractable thin-interface limit where (i) the width of the diffuse interface is about one order of magnitude smaller than the radius of curvature of the interface but much larger than the real microscopic width of a solid-liquid interface, and (ii) kinetic effects are negligible. A recently derived anti-trapping current [A. Karma, Phys. Rev. Lett. **87**, 115701 (2001)] is used in the solute conservation equation to recover precisely local equilibrium at the interface and to eliminate interface stretching and surface diffusion effects that arise when the solutal diffusivities are unequal in the solid and liquid. Model results are first compared to analytical solutions for one-dimensional steady-state solidification. Two-dimensional thermo-solutal dendritic growth simulations with vanishing solutal diffusivity in the solid show that both the microstructural evolution and the solute profile in the solid are accurately modeled by the present approach. Results are then presented that illustrate the utility of the model for simulating dendritic solidification for the large ratios of the liquid thermal to solutal diffusivities (Lewis numbers) typical of alloys.

DOI: 10.1103/PhysRevE.69.051607 PACS number(s): 81.10.Aj, 81.30.Fb, 05.70.Ln, 64.70.Dv

I. INTRODUCTION

Most cast metals typically contain one or more solutes and predicting the evolution of the microstructure and segregation patterns of solidified alloys is of great technological interest. Solidification of alloys differs in many respects from solidification of pure substances. The solidification rate is limited by both heat and solute diffusion. The heat and solute diffusion fields are coupled at the solid-liquid interface by the relations for the interface temperature (e.g., phase diagram) and by heat and solute flux balances. Furthermore, the solutal diffusivity in the liquid state is generally two to four orders of magnitude smaller than the thermal diffusivity. Therefore, solute diffusion is often on a length scale similar to that of the microstructure (e.g., dendrites), and small solute additions can strongly affect the interface pattern evolution. Because of the low solutal diffusivity, larger solute additions tend to slow the solidification rate relative to that in pure substances. Another characteristic of alloy solidification is the large contrast of solutal transport properties in solid and liquid; the solutal diffusivity is typically two to four orders of magnitude smaller in solid than liquid. This contrast strongly influences the microsegregation pattern in the solid and hence the properties of solidified alloys. Despite its importance, direct numerical simulation of alloy solidification controlled by both solute and heat diffusion has experienced only limited progress.

The phase-field method has become a widely accepted technique for the computational modeling of interfacial pattern formation and has been the subject of several recent review articles [1,2]. Its most appealing feature is that explicit interface tracking is avoided by the introduction of an order parameter, i.e., a phase-field variable, which takes on constant values in the bulk phases and varies smoothly but steeply in a diffuse interface region. The heat and solute conservation equations are appropriately modified to account for the presence of heat and solute rejection inside the diffuse interface. Phase-field formulations involve new parameters that must be related to physically measurable properties. This is often done through a "sharp-interface" analysis, which considers the asymptotics of the model equations in the limit of vanishing interface width. Such a sharp-interface analysis requires that the interface width be of the order of the capillary length, which makes computations intractable because an exorbitantly fine grid is needed to resolve the steep gradients inside the diffuse interface.

This problem is circumvented to a large extent by the "thin-interface" analyses presented by Karma and Rappel [3,4] for pure substances and by Karma [5] for isothermal solidification of dilute binary alloys. These thin-interface analyses assume that the interfacial region is small compared to the scale of the microstructural pattern but much larger than the capillary length. References [4,5] illustrate the advantages of the thin-interface analyses and also show that the phase-field parameters can be chosen such that interface kinetic effects are eliminated.

Previous numerical studies of alloy solidification have often omitted to solve the heat equation, but employed various assumptions for the temperature, i.e., isothermal domain, constant cooling rate, "frozen gradient," etc. [6–9]. The model presented here is intended for small concentrations where, even though the thermal diffusivity may be much larger than the solutal diffusivity, the solutal and thermal

---

[*] Corresponding author.
Email address: becker@engineering.uiowa.edu

1539-3755/2004/69(5)/051607(16)/$22.50

effects are still comparable and the solute and heat conservation equations need to be solved simultaneously. Recently, a study of nonisothermal binary alloy solidification using the phase-field method has been presented [10] but the authors report the presence of solute trapping and interface width dependent results. In Ref. [11], the model of Loginova *et al.* [10] is used together with an adaptive finite volume mesh that allows dendrites to grow without the thermal boundary layer reaching the boundaries. However, Ref. [11] also reports the lack of convergence of results with interface width and the presence of solute trapping. The phase-field model set forth in the present work uses a computationally tractable thin-interface analysis that makes it possible to obtain results that are independent of the interface width and that provides the freedom to choose the phase-field parameters such that growth without kinetic effects or solute trapping can be simulated.

This paper is organized as follows. In Sec. II the sharp-interface model of alloy solidification is reviewed. The phase-field model is introduced in Sec. III and the thin-interface limit is presented in Sec. IV. A comparison of phase-field results with an analytical sharp-interface solution for a one-dimensional solidification system is given in Sec. V. The model is further validated by comparing it to the two-dimensional calculations of Karma [5] for purely solutal (isothermal) dendritic growth. Finally, several two-dimensional dendritic growth simulations are presented for the case of coupled heat and solute diffusion with Lewis numbers of unity and 50. Independence of the results on the diffuse interface width and the grid spacing is demonstrated.

II. SHARP-INTERFACE MODEL

Consider the solidification of a dilute binary alloy with equal thermal diffusivity (α) and specific heat at constant pressure (c_p) in solid and liquid, and zero solid-state solutal diffusivity. The standard set of sharp-interface equations consists of

$$\partial_t c = D\nabla^2 c \quad \text{(liquid)}, \tag{1}$$

$$\partial_t T = \alpha\nabla^2 T \quad \text{(liquid and solid)}, \tag{2}$$

$$c_l(1-k)V_n = -D\partial_n c_l \quad \text{(mass conservation)}, \tag{3}$$

$$LV_n = c_p\alpha(\partial_n T|_s - \partial_n T|_l) \quad \text{(heat conservation)}, \tag{4}$$

$$T_l = T_M + mc_l - \Gamma\kappa - V_n/\mu_k \quad \text{(Gibbs-Thomson)}, \tag{5}$$

where c is the mole fraction of B (solute) atoms, D is the solutal diffusivity in the liquid, T is the temperature field, c_l is the concentration on the liquid side of the interface, k is the equilibrium partition coefficient, V_n is the normal velocity of the interface, L is the latent heat, T_l is the temperature on the liquid side of the interface, T_M is the melting point of pure solvent, m is the liquidus slope of the dilute alloy phase diagram, Γ is the Gibbs-Thomson coefficient, κ is the local curvature of the interface, and μ_k is the kinetic coefficient.

To relate the sharp-interface and phase-field models later on, it is convenient to define the dimensionless variables

$$U = \frac{c - c_\infty}{(1-k)c_\infty}, \tag{6}$$

$$\theta = \frac{T - T_m - mc_\infty}{L/c_p}, \tag{7}$$

where c_∞ is the value of c far from the interface that equals the initial concentration of the alloy. According to the above definitions, U and θ are dimensionless measures of the concentration and the undercooling, respectively.

In terms of these variables, the free-boundary problem becomes

$$\partial_t U = D\nabla^2 U, \tag{8}$$

$$\partial_t \theta = \alpha\nabla^2\theta, \tag{9}$$

$$[1 + (1-k)U_i]V_n = -D\partial_n U|_l, \tag{10}$$

$$V_n = \alpha(\partial_n\,\theta|_s - \partial_n\,\theta|_l), \tag{11}$$

$$\theta_i + Mc_\infty U_i = -d_0\kappa - \beta V_n, \tag{12}$$

where the thermal capillary length is defined as

$$d_0 = \frac{\Gamma}{L/c_p} = \frac{\gamma T_M c_p}{L^2}, \tag{13}$$

and γ is the excess free energy of the solid/liquid interface; for simplicity, we take γ to be isotropic to construct the phase-field model and introduce anisotropy later on for the dendrite growth simulations. Additionally, we have defined the kinetic coefficient

$$\beta = \frac{c_p}{\mu_k L}, \tag{14}$$

and the scaled magnitude of the liquidus slope

$$M = \frac{-m(1-k)}{L/c_p}. \tag{15}$$

Note that the subscript i on θ and U is present when these quantities are being evaluated at the interface (the liquid side for U). In the following section a variable U is defined in the phase-field model that is related to the chemical potential (and hence is continuous at the interface) and that is identical to the definition of Eq. (6) in the liquid.

III. PHASE-FIELD MODEL

The objective is to construct a phase-field model that reduces to the above set of sharp-interface equations in a computationally tractable thin-interface limit where (i) the width W of the diffuse interface is mesoscopic, i.e., W is about one order of magnitude smaller than the radius of curvature of the interface (e.g., the dendrite tip radius) but much larger than the real microscopic width of a solid-liquid interface, and (ii) kinetic effects are negligible ($\beta=0$) as for many alloys solidified at small undercooling/supersaturation. We first motivate the phase-field equations from a thermodynamic viewpoint and then analyze the thin-interface limit of these equations by a direct extension of recent results for the isothermal solidification of a dilute alloy [5].

The starting point of the model is an expression for the total free energy of the system that can be written in the form

$$F[\phi,c,T] = \int dV\left[\frac{\sigma}{2}|\nabla\phi|^2 + f_{AB}(\phi,c,T)\right], \qquad (16)$$

where $f_{AB}(\phi,c,T)$ denotes the bulk free energy density of a binary mixture of A and B atoms/molecules and c denotes the solute concentration defined as the mole fraction of B.

The phase-field equations considered are

$$\frac{\partial\phi}{\partial t} = -K_\phi\frac{\delta F}{\delta\phi}, \qquad (17)$$

$$\frac{\partial c}{\partial t} = \vec{\nabla}\cdot\left(K_c\vec{\nabla}\frac{\delta F}{\delta c} - \vec{j}_{at}\right), \qquad (18)$$

$$\frac{\partial T}{\partial t} = \alpha\nabla^2 T + \frac{L}{2c_p}\frac{\partial\phi}{\partial t}, \qquad (19)$$

where K_c and K_ϕ are constants. Equation (18) is equivalent to the mass continuity relation with $\mu\equiv\delta F/\delta c$ identified as the chemical potential. The solute current consists of two parts. The first $-K_c\vec{\nabla}\mu$ is the standard flux driven by the gradient of chemical potential that reduces to Fick's law of diffusion in the liquid. The second $\vec{j}_{at}$ is an "antitrapping" current that is only nonvanishing in the diffuse interface region [5], and hence does not affect the bulk thermodynamic properties of the model that remain governed by F. This current produces a solute flux from solid to liquid along a direction normal to the interface ($\hat{n}=-\vec{\nabla}\phi/|\vec{\nabla}\phi|$) that counterbalances the solute flux induced by the gradient of chemical potential across a moving interface. The latter leads to the well-known effect of solute trapping that has been studied experimentally [12] and reproduced previously in a phase-field model [13]. The characteristic velocity for solute trapping, which is proportional to D/W [12,13], is reduced abnormally for a thick interface (large W) in the simulations [5]. The form and magnitude of the antitrapping current can be chosen so as to eliminate this spurious effect and to recover precisely local equilibrium at the interface. Furthermore, this current provides sufficient flexibility in the choice of functions in the phase-field model to eliminate corrections to the mass conservation condition (interface stretching and surface diffusion) that arise in the thin-interface limit when the solute diffusivities are unequal in solid and liquid [5,14] (and Ref. [15] for the two-sided thermal model). Note that it is possible to write down the phase-field model in a form where the temperature equation is also derived variationally by introducing the energy density as an auxiliary variable. However, this is unnecessarily complicated here since the antitrapping current already makes the equations nonvariational. Our main goal is to formulate the phase-field model in such a way as to solve the sharp-interface equations written down in the preceding section in some computationally tractable limit. A nonvariational formulation has proven to be more flexible for this purpose [5].

A form of the free energy density appropriate for the dilute limit $c\ll 1$ is used that has the advantage that it leads to simple analytical forms for the stationary phase-field and solute profiles across the diffuse interface [1] and a constant γ. The bulk free-energy density of the alloy $f_{AB}(\phi,c,T)$ is written as the sum of the free energy of the pure material $f(\phi,T)$ and the contribution due to solute addition. The latter is the sum of the standard entropy of mixing $RT\nu_0^{-1}(c\ln c-c)$, where R is the universal gas constant and ν_0 is the molar volume assumed constant, and the change $\varepsilon(\phi)c$ of the energy density due to solute addition. The choice

$$\varepsilon(\phi) = \frac{1+\overline{g}(\phi)}{2}\varepsilon_s + \frac{1-\overline{g}(\phi)}{2}\varepsilon_l, \qquad (20)$$

interpolates between the values ε_s and $\varepsilon_l<\varepsilon_s$ in the solid and liquid, respectively, where $\overline{g}(\phi)$ is a monotonously increasing function of ϕ with limits $\overline{g}(\pm1)=\pm1$, with $\phi=+1(\phi=-1)$ corresponding to solid (liquid). Adding together the pure and solute contributions yields

$$f_{AB}(\phi,c,T) = f(\phi,T_M) + f_T(\phi)\Delta T + \frac{RT_M}{\nu_0}(c\ln c-c) + \overline{\varepsilon}c + \overline{g}(\phi)\frac{\Delta\varepsilon}{2}c, \qquad (21)$$

where

$$f(\phi,T_M) = H(-\phi^2/2+\phi^4/4), \qquad (22)$$

has the standard form of a double-well potential with a barrier height H and $\overline{\varepsilon}\equiv(\varepsilon_s+\varepsilon_l)/2$ and $\Delta\varepsilon\equiv\varepsilon_s-\varepsilon_l$ have been defined. Moreover, the pure part has been expanded to first order in $\Delta T\equiv T-T_M$ by defining the function $f_T(\phi)\equiv\partial f(\phi,T)/\partial T|_{T=T_M}$, and RT/ν_0 has been replaced by RT_M/ν_0 since terms $\sim\Delta T_c$ can be neglected in the dilute limit. Other phase-field models are derived with expressions for the bulk free energy that are not restricted to the dilute limit [7,9]. For example, the model introduced in Ref. [9] describes the solidification of a binary alloy with a lens-shaped phase diagram. Also, Kim and co-workers [7] have shown that, in the dilute limit, their model reduces to that of Tiaden *et al.* [6].

Next, the equilibrium properties of the model follow from the equations,

$$\frac{\delta F}{\delta c} = \mu_E, \qquad (23)$$

$$\frac{\delta F}{\delta\phi} = 0, \qquad (24)$$

where μ_E is the spatially uniform equilibrium value of the chemical potential. These two conditions uniquely determine the spatially varying stationary profiles of c and ϕ in the diffuse interface region, $c_0(x)$ and $\phi_0(x)$. The c profile varies between the equilibrium concentration $c_s^0(T)[c_l^0(T)]$ in the solid (liquid) phase, which define the equilibrium phase diagram of the alloy. These concentrations are determined by the standard common tangent construction that follows directly from Eqs. (23) and (24). The latter is equivalent to requiring that the chemical potential and the grand potential (i.e., thermodynamic potential for a varying number of solute particles) be equal in the solid and liquid, or, respectively,

$$\left.\frac{\partial f_s(c,T)}{\partial c}\right|_{c=c_s^0} = \left.\frac{\partial f_l(c,T)}{\partial c}\right|_{c=c_l^0} = \mu_E, \tag{25}$$

$$f_s(c_s^0,T) - \mu_E c_s^0 = f_l(c_l^0,T) - \mu_E c_l^0. \tag{26}$$

Applying the first equilibrium condition (23), we obtain at once

$$\frac{RT_M}{\nu_0}\ln c + \bar{\varepsilon} + \bar{g}(\phi)\frac{\Delta\varepsilon}{2} = \mu_E, \tag{27}$$

from which the expressions for the equilibrium partition coefficient

$$k \equiv \frac{c_s^0}{c_l^0} = \exp\left(-\frac{\nu_0\Delta\varepsilon}{RT_M}\right), \tag{28}$$

and the stationary concentration profile

$$c_0(x) = c_l^0 \exp\left(\frac{\ln k}{2}\{1 + \bar{g}[\phi(x)]\}\right), \tag{29}$$

are obtained. Now, applying the second equilibrium condition (24), yields

$$\sigma\frac{d^2\phi_0}{dx^2} + H(\phi_0 - \phi_0^3) = f_T'(\phi_0)\Delta T + \bar{g}'(\phi_0)\frac{\Delta\varepsilon}{2}c_0, \tag{30}$$

where the primes denote differentiation with respect to ϕ. If the function $f_T(\phi)$ is chosen of the form

$$f_T(\phi) = \frac{RT_M}{\nu_0 m}\exp\left(\frac{\ln k}{2}[1 + \bar{g}(\phi)]\right), \tag{31}$$

the right-hand side of Eq. (30) vanishes provided that

$$T = T_M + mc_l^0. \tag{32}$$

It should be noted that Eq. (31) recovers standard thermodynamics of dilute alloys. Indeed, since $f_T(+1) - f_T(-1) = L/T_M$ [1], the right-hand side of Eq. (31) is such that the Van't Hoff relation

$$\frac{L}{T_M} = \frac{RT_M(1-k)}{\nu_0 m}, \tag{33}$$

is recovered by subtracting Eq. (31) evaluated at $\phi = +1$ from the same equation evaluated at $\phi = -1$. This relation is a special case of the Gibbs-Konovalov rule when applied to dilute alloys [16].

The vanishing of the right-hand side of Eq. (30) implies that $\phi_0(x) = -\tanh[x/(\sqrt{2}W)]$ where W measures the width of the diffuse interface. In addition, for Eq. (18) to reduce to Fick's law of diffusion in the liquid, the form

$$K_c = \frac{\nu_0}{RT_M}Dq(\phi)c \tag{34}$$

is chosen, where $q(\phi)$ is a dimensionless function that dictates how the solute diffusivity varies through the diffuse interface. With all the above choices, Eqs. (17) and (18) become

$$\tau\frac{\partial\phi}{\partial t} = W^2\nabla^2\phi + \phi - \phi^3 + \frac{RT_M \ln k}{\nu H}\bar{g}'(\phi) \times\left[c - \frac{T - T_M}{m}\exp\left(\frac{\ln k}{2}[1 + \bar{g}(\phi)]\right)\right], \tag{35}$$

$$\frac{\partial c}{\partial t} = \vec{\nabla}\cdot\left(Dq(\phi)c\vec{\nabla}\left[\ln c - \frac{\ln k}{2}\bar{g}(\phi)\right] - \vec{j}_{at}\right), \tag{36}$$

where $\tau = 1/(K_\phi H)$ has also been defined and Eq. (19) is unchanged. To make contact with the results of Ref. [5] for the isothermal limit where T is constant, the above equations are rewritten in terms of the dimensionless variable

$$u = \frac{\nu_0}{RT_M}(\mu - \mu_\infty) = \ln(c/c_\infty) - \frac{\ln k}{2}[\bar{g}(\phi) + 1], \tag{37}$$

which measures the departure of the chemical potential from its value μ_∞ for a flat interface at the equilibrium liquidus temperature. In addition, $\bar{g}(\phi)$ is eliminated in favor of the function $\tilde{g}(\phi)$, which has the same limits $\tilde{g}(\pm 1) = \pm 1$, using the transformation

$$\exp\left(\frac{\ln k}{2}[1 + \bar{g}(\phi)]\right) = \frac{1+k}{2} - \frac{1-k}{2}\tilde{g}(\phi). \tag{38}$$

After simple algebraic manipulations, Eqs. (35) and (36) become

$$\tau\frac{\partial\phi}{\partial t} = W^2\nabla^2\phi + \phi - \phi^3 - \frac{RT_M(1-k)c_\infty}{2\nu_0 H}\tilde{g}'(\phi) \times\left(\exp(u) - \frac{T - T_M}{mc_\infty}\right), \tag{39}$$

$$\frac{\partial c}{\partial t} = \vec{\nabla}\cdot[D_q(\phi)c\vec{\nabla}u - \vec{j}_{at}], \tag{40}$$

where $u = \ln\big(2(c/c_\infty)/[1 + k - (1-k)\tilde{g}(\phi)]\big)$. As discussed in Ref. [5], additional freedom to obtain the desired thin-interface limit can be gained by replacing the function $\tilde{g}(\phi)$ in this last expression for u by another function $h(\phi)$ that has the same limits at $\phi = \pm 1$. The simplest choice is $h(\phi) = \phi$, which yields the new expression

$$u = \ln\left(\frac{2c/c_\infty}{1+k-(1-k)\phi}\right). \tag{41}$$

The phase-field model is now completely defined by Eqs. (39)–(41) and (19), together with the additional choices

$$\vec{j}_{at} = -\frac{c_\infty(1-k)W}{2\sqrt{2}}\exp(u)\frac{\partial\phi}{\partial t}\frac{\vec{\nabla}\phi}{|\vec{\nabla}\phi|}, \tag{42}$$

$$q(\phi) = \frac{1-\phi}{1+k-(1-k)\phi}. \tag{43}$$

The model defined by Eqs. (39)–(43) yields the desired thin-interface limit as discussed in the following section and the Appendix. It is interesting to note that the present thermodynamically motivated phase-field model is identical, with the exception of the antitrapping current in the species equation and the choice of the function $\tilde{g}(\phi)$ in Eq. (39), to that of Beckermann *et al.* [8], which was derived with a geometrically motivated volume-averaging technique.

IV. THIN-INTERFACE LIMIT

To analyze the thin-interface limit of this model, as well as to carry out simulations, it is useful to rewrite the phase-field equations in terms of the dimensionless thermal undercooling θ defined by Eq. (7), as well as the variable

$$U = \frac{\exp(u)-1}{1-k}, \tag{44}$$

which reduces to the dimensionless concentration defined by Eq. (6) on the liquid side of the interface ($\phi=-1$). The following final set of equations is obtained

$$\tau\frac{\partial\phi}{\partial t} = W^2\nabla^2\phi + \phi - \phi^3 - \lambda g'(\phi)(\theta + Mc_\infty U), \tag{45}$$

$$\frac{1+k}{2}\frac{\partial U}{\partial t} = \vec{\nabla}\cdot\left(D\frac{1-\phi}{2}\vec{\nabla}U + \frac{W}{2\sqrt{2}}[1+(1-k)U]\frac{\partial\phi}{\partial t}\frac{\vec{\nabla}\phi}{|\vec{\nabla}\phi|}\right) + \frac{1}{2}\frac{\partial}{\partial t}\{\phi[1+(1-k)U]\}, \tag{46}$$

$$\frac{\partial\theta}{\partial t} = \alpha\nabla^2\theta + \frac{1}{2}\frac{\partial\phi}{\partial t}, \tag{47}$$

where the coupling constant λ is defined as

$$\lambda = -\frac{15}{8}\frac{RT_M(1-k)L}{2\nu_0 Hc_p m} = \frac{15L^2}{16Hc_pT_M}, \tag{48}$$

and $g(\phi)=8\tilde{g}(\phi)/15$. The factor of 15/8 has been introduced such that for the choice $\tilde{g}(\phi)=15(\phi-2\phi^3/3+\phi^5/5)/8$ and $g'(\phi)=(1-\phi^2)^2$, Eqs. (45)–(47) above reduce identically to those analyzed by Karma and Rappel [3,4] in the limit of vanishing concentration $Mc_\infty\to 0$. Also $1/\lambda$ is a dimensionless measure of the barrier height of the double-well potential, and the second equality in Eq. (48) follows from the Van't Hoff relation for dilute alloys, Eq. (33).

An asymptotic analysis of the thin-interface limit of this model is needed to show that it reduces to the free-boundary problem defined by Eqs. (8)–(12). The basic results of this analysis have already been summarized for the isothermal limit in Ref. [5]. Given that the treatment of the isothermal and the thermosolutal case are very similar, all the mathematical details of the analysis need not be repeated here. The main difference between the two cases is the expression for the interface kinetic coefficient β that is derived in the Appendix for a one-dimensional interface. As in the isothermal limit, corrections to the mass conservation condition that correspond to interface stretching and surface diffusion vanish in the present thermosolutal model. The expressions for d_0 and β that are necessary to carry out the simulations, are given in the following.

The excess free energy of the solid-liquid interface is given by

$$\gamma = WH\int_{-\infty}^{+\infty} dy\left(\frac{d\phi_0}{dy}\right)^2 \equiv IWH, \tag{49}$$

where y is the coordinate along the direction normal to the interface scaled by W, and $I=2\sqrt{2}/3$ is obtained by evaluating the integral with $\phi_0=-\tanh[y/(\sqrt{2}W)]$. Note that the fact that γ is independent of concentration in the present model is a direct consequence of our choice of the free-energy density that uncouples the equilibrium phase field and concentration profiles in the diffuse interface. From the definitions of the capillary length, Eq. (13), and of λ, Eq. (48), one obtains at once that

$$d_0 = a_1\frac{W}{\lambda}, \tag{50}$$

where $a_1=15I/16=0.8839\ldots$. The equations of the present phase-field model reduce identically to those analyzed by Karma and Rappel [3,4] in the limit of vanishing concentration $Mc_\infty\to 0$, as well as to those analyzed by Karma [5] in the isothermal case where θ is fixed.

The expression for β can be derived by applying the same analyses as those presented in Refs. [3–5] to derive a relationship between the planar interface velocity V and the thermodynamic driving force at the interface $\theta_i+Mc_\infty U_i$ in the present thermosolutal model. As detailed in the Appendix, this analysis is considerably simplified by the fact that both θ and U have similar spatial variations in the diffuse interface region at leading order in an asymptotic expansion where the interface Péclet number $p=WV/D$ is the small parameter, or equivalently at second order in an expansion where λ is the small parameter [4,14]. This similarity is a direct consequence of the forms chosen for the antitrapping current, Eq. (42), and of the diffusivity function $q(\phi)$, Eq. (43), and is key to recover the desired thin-interface limit without corrections to the solute or heat conservation conditions at the interface and with local chemical equilibrium at the interface. The expression for β is given by

$$\beta = a_1\left(\frac{\tau}{W\lambda} - a_2\frac{W}{D}\left[\frac{D}{\alpha} + Mc_\infty[1+(1-k)U]\right]\right), \quad (51)$$

where a_2 is a constant that depends on the choice of the function $g(\phi)$. In this paper the standard form $g(\phi)=\phi-2\phi^3/3+\phi^5/5$ will be used, which has vanishing first and second derivatives at $\phi=\pm1$, for which $a_2=0.6267\ldots$ [4]. The whole term multiplying a_2 originates from the fact that both θ and U are spatially varying in the diffuse interface region, i.e., $\beta=a_1\tau/W\lambda$ with both α and D tending to infinity and hence both θ and U constant through the interface. Note that for a realistic value of D/α, this term is largely dominated by the spatial variation of U, or equivalently of the chemical potential, through the interface. This is because θ varies on a scale α/V that is several orders of magnitude larger than the scale D/V over which U varies. Hence, θ is essentially constant inside the diffuse interface when both $\alpha/D \gg 1$ and $D/V \gg W$. It should be pointed out that in Ref. [5], the U appearing in the expression for β is taken to be a constant rather than the actual field. The constant value of U that was used in Ref. [5] to evaluate β was the value corresponding to a sharp, flat interface under equilibrium conditions at the interface temperature, which was known because solidification was assumed to occur isothermally. This stands in contrast to a thermosolutal situation where there is no way of knowing the interface temperature *a priori*.

It follows from Eq. (51) that β can be made to vanish provided that τ is chosen to be a function of U in the phase-field model, defined by

$$\tau(U) = a_2\lambda\frac{W^2}{D}\left[\frac{D}{\alpha} + Mc_\infty[1+(1-k)U]\right]. \quad (52)$$

As in previous studies, crystalline anisotropy is included, by letting $W=W_0A(\hat{n})$, where $\hat{n}=-\vec{\nabla}\phi/|\vec{\nabla}\phi|$ is the unit vector normal to the interface and $A(\hat{n})=1+\varepsilon\cos 4\varphi$ is a function that describes the anisotropy, where $\varphi=\arctan(\partial_y\phi/\partial_x\phi)$ is the angle between the direction normal to the interface and the x (horizontal) axis, and ε is a dimensionless parameter that characterizes the anisotropy strength. To carry out the simulations, it is useful to define the scaled diffusivity

$$\tilde{D} = \frac{D\tau_0}{W_0^2} \quad (53)$$

and the Lewis number

$$\mathrm{Le} = \frac{\alpha}{D}. \quad (54)$$

Following Eq. (52), β can be made to vanish by inputting into the phase-field model

$$\tau(U,\vec{\nabla}\phi/|\vec{\nabla}\phi|) = \tau_0[A(\vec{\nabla}\phi/|\vec{\nabla}\phi|)]^2 \times\left[\frac{1}{\mathrm{Le}} + Mc_\infty[1+(1-k)U]\right], \quad (55)$$

and

$$\tilde{D} = \lambda a_2. \quad (56)$$

Measuring length and time in units of W_0 and τ_0, respectively, scales out these parameters from the phase-field equations, in which case the only parameters left are $\tilde{D}$, λ, and Le. The results can be related to physical units using the relation $W_0=d_0\lambda/a_1$ and $\tau_0=(d_0^2/D)a_2\lambda^3/a_1^2$ [which follow from Eqs. (50) and (53)]. The results should be independent of λ when they are converged. Note that decreasing λ corresponds physically to decreasing the interface width while increasing at the same time the height of the double-well potential so as to keep the surface energy and hence d_0 fixed.

V. VALIDATION FOR ONE-DIMENSIONAL STEADY-STATE ALLOY SOLIDIFICATION WITH KINETICS

A. Analytical solution for a sharp interface

An analytical solution of the sharp-interface model can be found for the steady-state propagation of a flat interface into a hypercooled melt of a binary alloy with kinetics, which provides a validation case for the phase-field model. The governing equations of the sharp-interface formulation are rewritten in a moving frame attached to the interface, which propagates with a constant velocity V along the sole coordinate x as

$$V\frac{\partial U}{\partial x} + D\frac{\partial^2 U}{\partial x^2} = 0, \quad (57)$$

$$V\frac{\partial \theta}{\partial x} + \alpha\frac{\partial^2 \theta}{\partial x^2} = 0, \quad (58)$$

together with the interface conditions

$$[1+(1-k)U_i]V = -D\partial_x U|_l, \quad (59)$$

$$V = -\alpha\partial_x\theta|_l, \quad (60)$$

$$\theta_i + Mc_\infty U_i = -\beta V, \quad (61)$$

and the far-field boundary conditions

$$\lim_{x\to\infty} U(x) = 0, \quad (62)$$

$$\lim_{x\to\infty} \theta(x) = -\Delta, \quad (63)$$

where Δ denotes an externally imposed dimensionless undercooling. The solution of Eqs. (57)–(63) is given by the following spatial distributions of U and θ

$$U = \frac{1}{k}\exp\left(-\frac{Vx}{D}\right), \quad (64)$$

$$\theta = \exp\left(-\frac{1}{\mathrm{Le}}\frac{Vx}{D}\right) - \Delta, \quad (65)$$

in the liquid and $U=1/k$ and $\theta=1-\Delta$ in the solid, and the expression for interface velocity

$$\beta V = \Delta - 1 - \frac{Mc_\infty}{k}. \tag{66}$$

Since the equilibrium freezing range corresponding to a melt concentration c_∞ is given by $-mc_\infty(1-k)/k$, the last term in Eq. (66) represents the freezing range nondimensionalized by the unit undercooling, L/c_p. For the solution to be valid, therefore, the imposed dimensionless undercooling must exceed unity.

Using Eqs. (6) and (64), the concentration distribution in the liquid is given by

$$c = c_\infty\left[1 + \frac{1-k}{k}\exp\left(-\frac{Vx}{D}\right)\right]. \tag{67}$$

The concentration distribution in the solid is $c = c_\infty$.

B. Comparison of phase field with analytical sharp-interface results

After nondimensionalization using $\tau = \tau_0$ as the time scale and $W = W_0$ as the length scale, one-dimensional versions of Eqs. (45)–(47) were solved numerically until a steady state was achieved. The equations were discretized with finite differences in space and explicit time stepping. The computational domain consisted of 2000 equally spaced grid points. The dimensionless grid spacing and time step used were $\Delta x/W_0 = 0.4$ and $\Delta t/\tau_0 = 0.008$, respectively. Zero-flux boundary conditions were imposed on both ends for the concentration field. For the temperature field, the left end was taken as insulated and on the right end a time dependent temperature, known from the analytical solution, was prescribed. The latter boundary condition allows one to choose a smaller computational domain for Le greater than unity because it eliminates the need to compute the entire thermal boundary layer. The initial condition consisted of a thin solid shell of concentration c_∞ and dimensionless temperature $1-\Delta$ at the left end of the domain, and liquid of concentration c_∞ at a prescribed undercooling, i.e., $\theta = -\Delta$, in the remainder. The interface was allowed to propagate to the right until the concentration boundary layer almost reached the right end of the domain (i.e., until the value of U at the next-to-last grid point increased to 10^{-3}). At this point, the profiles were shifted towards the left end of the domain and allowed to evolve in time again. This procedure was repeated until the interface velocity reached a constant, steady-state value.

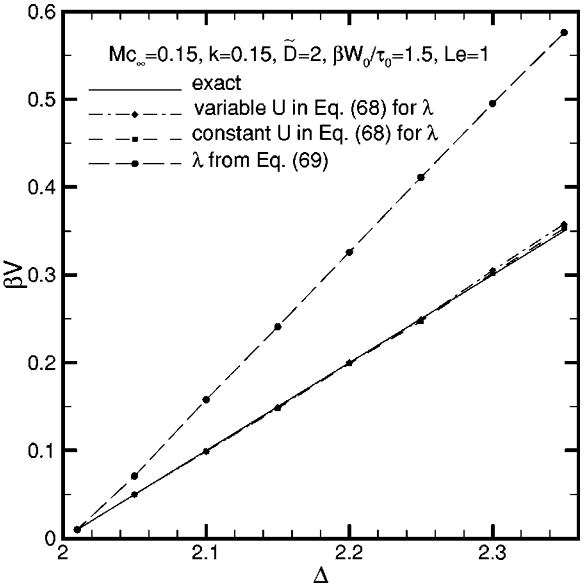

FIG. 1. Comparison of predicted (interrupted lines) and exact (solid line) interface velocities as a function of dimensionless thermal undercooling for one-dimensional solidification of a binary alloy into a hypercooled melt. The dashed and dash-dot lines are obtained with the thin-interface analysis; the long-dashed line corresponds to the sharp-interface analysis.

The coupling parameter λ as obtained from Eq. (51) as

$$\lambda = \frac{1}{\dfrac{\beta W_0}{a_1\tau_0} + \dfrac{a_2}{\tilde{D}}\left\{\dfrac{1}{\mathrm{Le}} + Mc_\infty[1+(1-k)U]\right\}}, \tag{68}$$

which implies that λ is a function of the concentration (i.e., U). According to Eq. (50), this causes the capillary length to be variable throughout the computational domain. However, the capillary length plays no physical role in the one-dimensional, flat interface problem considered here. The value of the scaled kinetic coefficient was taken as $\beta W_0/\tau_0 = 1.5$ and, in most cases, the Lewis number was set to unity. Furthermore, the values $Mc_\infty = 0.15$ and $k = 0.15$ were chosen such that the two terms in the curly brackets in Eq. (68), $1/\mathrm{Le}$ and $Mc_\infty[1+(1-k)U]$, are of a similar magnitude, and, consequently, thermal and solutal effects have the same impact on λ. The only free phase-field parameter is the scaled diffusivity $\tilde{D} = D\tau_0/W_0^2$, which is varied below in a convergence study.

The variation of the coupling parameter λ with U according to Eq. (68) deserves further attention. For the simple problem considered here, the equilibrium value of U at the (sharp) interface is known to be equal to $1/k$. This provides an opportunity to compare the performance of the phase-field model in the thin-interface limit for (i) a *variable U* in Eq. (68) for λ, where U is taken from the solution of Eq. (46), and (ii) a *constant* $U = 1/k$ in Eq. (68) for λ according to the method used in Ref. [5] for isothermal alloy solidification, as discussed in Sec. IV. A third method to calculate λ is given by the sharp-interface limit, i.e.,

$$\lambda_{sharp} = a_1\frac{\tau}{\beta W}, \tag{69}$$

which does not consider any spatial variations of U and θ within the diffuse interface. Equation (69) is obtained from Eq. (68) by setting $a_2 = 0$.

Figure 1 shows a comparison of the predicted interface speed as a function of undercooling with the analytical sharp-interface result, Eq. (66). It can be seen that for the thin-interface limit, both ways of computing the coupling parameter (variable or constant U) produce results that agree well with the exact solution, especially at lower undercoolings. The sharp-interface limit result for the coupling param-

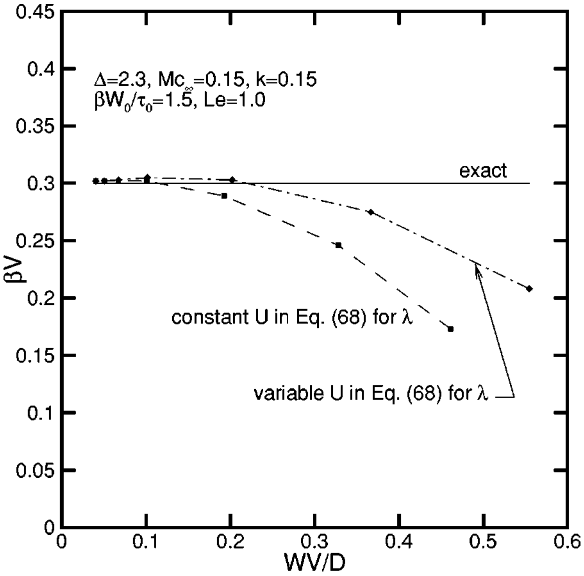

FIG. 2. Effect of interface solutal Péclet number, $\mathrm{Pe}_D = WV/D$, on predicted interface velocities for one-dimensional solidification of a binary alloy into a hypercooled melt. The solid horizontal line corresponds to the exact solution given by Eq. (66); the interrupted lines are from phase-field simulations using the thin-interface analysis for the coupling constant λ.

eter, on the other hand, produces results that are not in qualitative agreement with the exact solution. Equation (66) indicates that the steady-state velocity of the interface is independent of the Lewis number. This was verified numerically by simulating cases with large Le, which in some instances required using an implicit time discretization of the heat equation for numerical stability.

Figure 2 presents the results of a convergence study for one of the cases in Fig. 1 ($\Delta = 2.3$). Here, the predicted interface velocity is plotted against the interfacial solutal Péclet number WV/D. This Péclet number was varied by changing the scaled diffusivity $\tilde{D} = D\tau_0/W_0^2$ in the phase-field simulations. As expected from the thin-interface analysis (see Appendix), the predictions approach the exact solution for small interfacial solutal Péclet numbers. Physically, a small interfacial Péclet number corresponds to a small interface width relative to the diffusion length scale. If the interface width is too large, the thermal or solutal boundary layers will be inside the diffuse interface and cannot be accurately resolved. Note that both a constant and a variable U in Eq. (68) provide convergent results for smaller values of WV/D. The convergence behavior for a variable U is as good as or better than for a constant U.

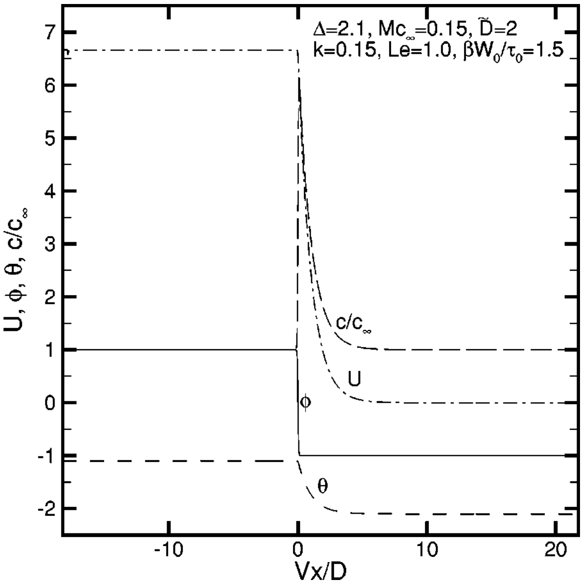

FIG. 3. Predicted steady-state profiles from a phase-field simulation of one-dimensional solidification of a binary alloy into a hypercooled melt; the entire computational domain is shown.

A comparison of predicted and exact temperature and solute concentration profiles is shown in Fig. 3. The interface is located at $Vx/D = 0$, with $Vx/D < 0$ being solid and $Vx/D > 0$ liquid; results for the entire computational domain are depicted. The mixture concentration in the dimensionless ratio c/c_∞ also plotted in Fig. 3 is defined as [8]

$$c = [(1-\phi)c_1 + (1+\phi)c_s]/2, \tag{70}$$

and can be calculated from U and phase-field profiles using Eqs. (44) and (41). This mixture concentration is equal to the solute concentration in the bulk solid and liquid phases and varies continuously inside the diffuse interface. The phase-field and analytical profiles are seen to be indiscernible on the scale of Fig. 3. Figure 4 shows a closeup of the interfacial region, where the difference between phase-field and analytical results can be better appreciated. This figure reveals how the temperature and U profiles from the phase-field model are smooth representations of kinks in these variables associated with the sharp-interface formulation. Figure 5 shows a similar closeup for various solute concentration profiles. The

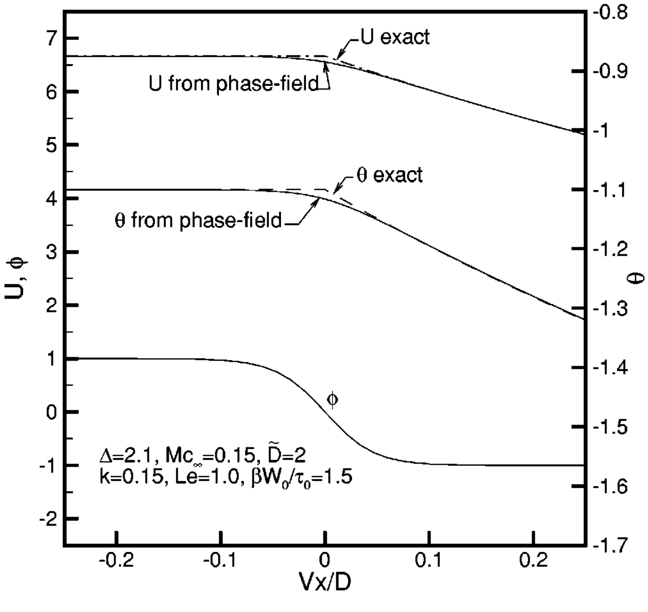

FIG. 4. Closeup of the dimensionless temperature, concentration, and phase-field profiles in Fig. 3 near the interface. The U and θ profiles predicted by the phase-field model vary smoothly inside the diffuse interface and match their sharp interface counterparts outside of it.

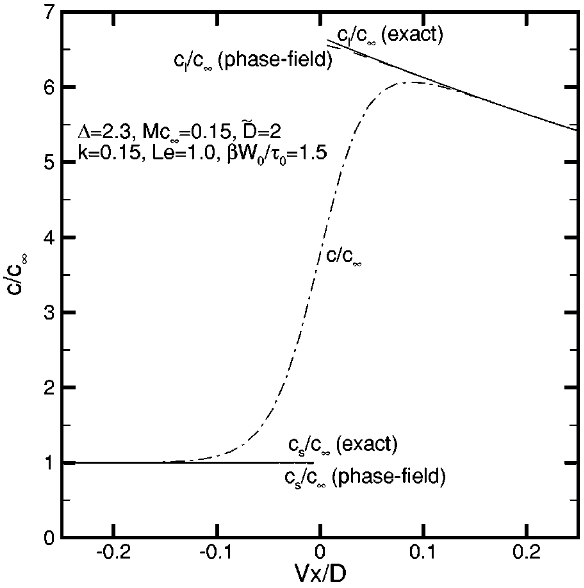

FIG. 5. Comparison of predicted (interrupted lines) and exact (solid lines) concentration profiles near the interface for the simulation of Fig. 3. The dash-dot line is the predicted mixture concentration that interpolates between the concentrations in the liquid and solid.

mixture concentration varies smoothly within the diffuse interface and approaches the concentration profiles in the bulk solid and liquid outside of it. The latter are obtained from the mixture concentration using the following relations $c_l/c_\infty = 2(c/c_\infty)/[1+k-(1-k)\phi]$ and $c_s/c_\infty = 2k(c/c_\infty)/[1+k-(1-k)\phi]$, which follow from Eq. (70). These bulk-phase concentration profiles from the phase-field model are seen in Fig. 5 to agree well with the analytical predictions from the sharp-interface model.

VI. SIMULATIONS OF ISOTHERMAL DENDRITIC SOLIDIFICATION

For further validation, the isothermal dendritic solidification of a binary alloy into a constitutionally undercooled melt is simulated in two dimensions and the results are compared to those presented by Karma [5]. The domain is a square box with symmetry boundary conditions applied on the bottom and left sides and a fixed far-field solute concentration at the right and top sides. The initial condition consists of a small, quarter-of-a-circle shaped solid seed in the lower left corner and undercooled melt in the remainder of the domain. The far-field concentration c_∞ and the equilibrium liquidus concentration at the system temperature, c_l^0, are related via the imposed solutal undercooling as

$$\Omega = \frac{c_l^0 - c_\infty}{(1-k)c_l^0}. \tag{71}$$

The following values of the system parameters were adopted from Ref. [5]: $\Omega=0.55$, $\varepsilon=0.02$, $k=0.15$, and no kinetic effect (i.e., $\beta=0$). For the calculation shown in Fig. 6, the value of the coupling constant was chosen as $\lambda=3.1913$, which corresponds to $\tilde{D}=2$. The governing equations were solved on a grid of 800×800 node points, with explicit time stepping and finite differences for the spatial derivatives. The grid size and the time step used were $\Delta x/W_0=0.4$ and $\Delta t/\tau_0=0.018$, respectively. Example results for the dendrite evolution, using the model of Karma [5], are shown in Fig. 6. The initial circular seed in the lower left corner grows into a dendrite with branches along the horizontal and vertical axes. The local radius of curvature at the tip of these branches is denoted by ρ and the tip propagation velocity by V.

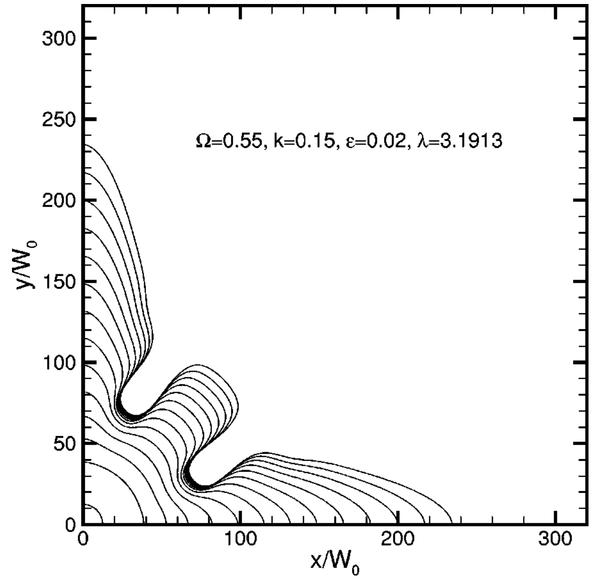

FIG. 6. Predicted interface contours, every 20 000 time steps, for two-dimensional, purely solutal (isothermal) dendritic solidification into an undercooled melt. The dendrite tip velocity is the rate at which the interface propagates along the horizontal axis and the dendrite tip radius is the local radius of curvature of the tip of the growing arm.

To simulate isothermal solidification of a binary alloy with the present model the Lewis number could, in principle, be set infinitely large. Needless to say, this is numerically unfeasible. Instead, the temperature was set to a given value θ_{sys} in the entire computational domain and the heat equation was not solved. In order to compare directly to the results of Ref. [5], which are presented in terms of the solutal capillary length $d_{0,s}=\gamma T_M/[L|m|(1-k)c_l^0]$, it is convenient to choose the parameters in the present model such that the solutal and thermal capillary lengths are equal, i.e., $d_{0,s}=d_0$. The ratio of the two capillary lengths is given by

$$\frac{d_{0,s}}{d_0} = \frac{(L/c_p)}{-m(1-k)c_l^0} = \frac{1-(1-k)\Omega}{Mc_\infty}, \tag{72}$$

where the second equality follows from Eqs. (15) and (71). Hence, when Mc_∞ and θ_{sys} are chosen as

$$Mc_\infty = 1-(1-k)\Omega \tag{73}$$

and

$$\theta_{sys} = -Mc_\infty \frac{\Omega}{1-(1-k)\Omega}, \tag{74}$$

respectively, the solutal and thermal capillary lengths are equal. For the case shown in Ref. [5], for which $k=0.15$ and $\Omega=0.55$, Eqs. (73) and (74) yield $Mc_\infty=0.5325$ and $\theta_{sys}=-\Omega=-0.55$.

The dendritic growth simulations performed using the present model correspond to a vanishing interface kinetic coefficient. Therefore, the relaxation time τ in the phase-field equation must be calculated from Eq. (55), which shows that τ is a function of U. As discussed above, the value of U in Eq. (55) is taken as a constant in Ref. [5], corresponding to the liquidus concentration at the system temperature c_l^0. Using Eqs. (6) and (71) it is easy to show that this constant value of U is given by $\Omega/[1-(1-k)\Omega]$. In summary, the present model should produce the same results as that of Ref. [5] if the temperature is set as $\theta_{sys}=-\Omega$, the initial melt concentration is chosen as $Mc_\infty=1-(1-k)\Omega$, and U in Eq. (55) is taken as $\Omega/[1-(1-k)\Omega]$.

Simulations were performed to study the convergence behavior for decreasing values of the coupling constant λ (and, consequently, of the scaled interface width W_0/d_0) and to examine the differences in the convergence behavior for a constant and variable U. The radius of the initial circular solid seed was $44d_0$ in all cases considered. The grid spacing was chosen as $\Delta x/W_0=0.4$, and the time step was varied depending on λ, to ensure numerical stability. For the values of $\lambda=1.5957, 3.1913, 6.3826, 9.574$, and 12.765 the time steps used were $\Delta t/\tau_0=0.016, 0.018, 0.008, 0.006$, and 0.0048, respectively. The computational domains were adjusted to have the same physical size in each case, resulting in 1600×1600, 800×800, 400×400, 267×267, and 200×200 nodal points for $\lambda=1.5957, 3.1913, 6.3826, 9.574$, and 12.765, respectively.

Figure 7 shows the predicted variation of the dendrite tip velocity with the coupling parameter λ. The velocities in Fig. 7 are all evaluated at the same dimensionless elapsed time of $tD/d_0^2=48\,000$. For the smallest three values of λ, this elapsed time is sufficient to achieve a steady-state growth regime. For $\lambda=9.574$ and $\lambda=12.765$, however, a steady state is not quite achieved because of the onset of interactions between the diffusion field and the far-field boundary. The cases with $\lambda=3.1913$ and $\lambda=6.3826$ were also simulated with the model of Ref. [5] and the results were found to agree exactly with those of the present model using a constant U in Eq. (55). It can be seen from Fig. 7 that the predicted dendrite tip velocities converge to a constant value with decreasing λ. Compared to using a constant U in Eq. (55), the convergence behavior appears to be slightly worse for a variable U. Nevertheless, the difference between the two cases decreases with decreasing λ.

Figure 8 shows the results of a grid independence study for the $\lambda=3.1913$ case in Fig. 7. The values of $\Delta x/W_0$ considered were 0.3, 0.4, 0.6, 0.8, and 1.0. For those respective cases the time steps were $\Delta t/\tau_0=0.01, 0.018, 0.03, 0.06$, and 0.1, and the domains were squares with 1060×1060, 800×800, 530×530, 400×400, and 320×320 nodal points. For both methods of computing the relaxation time τ [i.e., variable and constant U in Eq. (55)], it can be seen that the tip velocity at $tD/d_0^2=48\,000$ changes negligibly when $\Delta x/W_0$ is smaller than about 0.4.

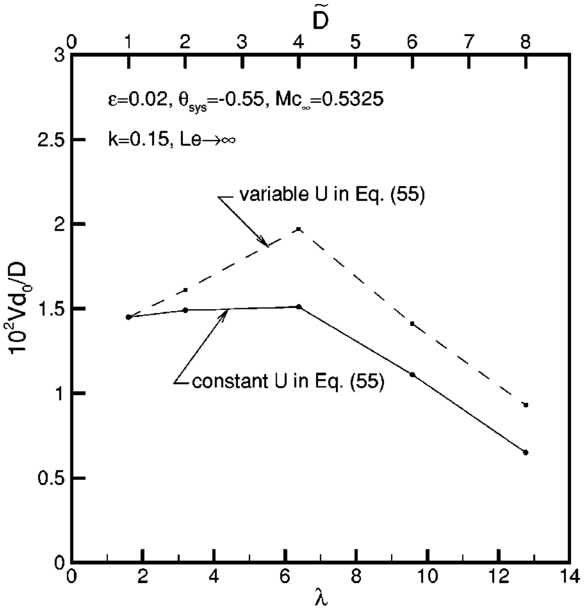

FIG. 7. Predicted dimensionless tip velocities as a function of λ (i.e., interface width) and two choices of computing the relaxation time, for two-dimensional, isothermal dendritic solidification of a binary alloy into an undercooled melt. All simulations have the same physical domain and initial seed sizes, and the tip velocities are evaluated at a time of $tD/d_0^2=48\,000$, which is near steady state.

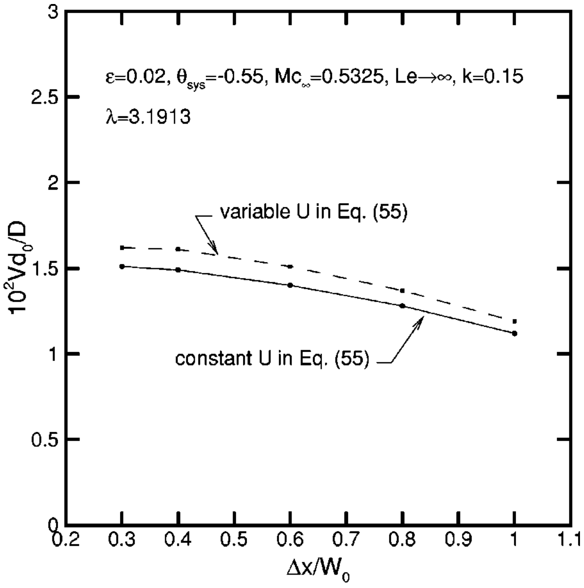

FIG. 8. Predicted dimensionless tip velocities as a function of grid spacing and two choices of computing the relaxation time, for two-dimensional, isothermal dendritic solidification of a binary alloy into an undercooled melt. All simulations have the same physical domain and initial seed sizes, and the tip velocities are evaluated at a time of $tD/d_0^2=48\,000$, which is near steady state.

VII. SIMULATIONS OF THERMOSOLUTAL DENDRITIC GROWTH

Next, the phase-field model is used to simulate nonisothermal dendritic growth in two dimensions of a binary alloy into an undercooled melt with coupled heat and solute diffusion. Only cases with vanishing interface kinetic coefficient are considered, and the phase-field relaxation time is computed using Eq. (55). Since the interfacial temperatures and concentrations are unknown, the variable U must be used in Eq. (55).

First, a convergence study is presented for $\mathrm{Le}=1$. The other physical parameters were chosen as $Mc_\infty=0.5325$, $k=0.15$, $\varepsilon=0.02$, and $\Delta=0.55$. With these values, the terms $1/\mathrm{Le}$ and $Mc_\infty[1+(1-k)U]$ in Eq. (55) for the phase-field relaxation time are of approximately the same order of magnitude. As the initial condition, a quarter-of-a-circle solid seed of radius $65d_0$ was placed in the lower left corner of a square box with a side length of $1730d_0$. Symmetry boundary conditions were applied at the bottom and left boundaries, while the top and right boundaries had constant far-field values of -1, $-\Delta$, and 0 prescribed for ϕ, θ, and U, respectively. The governing equations were solved with finite differences approximations and explicit time stepping. Four different values of λ (and hence, interface width) were examined, namely, $\lambda=3.1913, 6.3826, 9.574$, and 12.7653, corresponding to $\tilde{D}=2,4,6$, and 8, respectively. The grid size was always $\Delta x/W_0=0.4$. In order to represent the same physical length of $1730d_0$, the grid sizes used are 1200×1200, 600×600, 400×400, and 300×300 for $\lambda=3.1913, 6.3826, 9.574$, and 12.7653, respectively, while the time steps for these respective values of λ were taken as $\Delta t/\tau_0=0.018, 0.008, 0.006$, and 0.0048.

Figures 9(a) through 9(d) show the predicted time evolutions of the dimensionless dendrite tip velocity Vd_0/D, tip radius ρ/d_0, selection parameter σ^*, and ratio of tip radius to interface width ρ/W_0, respectively. The selection parameter is defined here as $\sigma^*=2Dd_0/(\rho^2V)$, and should simply be viewed as a dimensionless inverse product of ρ^2V; detailed comparisons with available dendrite tip selection theories are beyond the scope of the current study. Note that in Fig. 9 the dendrite tip does not reach a steady-state growth regime because of the limited size of the domain. In particular, the tip velocity [Fig. 9(a)] shows a marked increase when the thermal and solutal boundary layers start to interact with the far-field domain boundaries. The increase is due to the use of fixed far-field temperature and concentration values as the boundary condition. The different lines within the plots correspond to simulations performed for different values of the free parameter λ. It is clear from Figs. 9(a)–9(c) that the results converge for decreasing λ. The plot of ρ/W_0 [Fig. 9(d)] and the proximity of the curves for $\lambda=3.1913$ and $\lambda=6.3826$ in Figs. 9(a)–9(c) suggest that the ratio ρ/W_0 should be greater than about 10 to obtain converged results.

Another test of the accuracy of the present results is performed by comparing the predicted frozen solute profile along the dendrite axis with interfacial concentrations calculated from the Gibbs-Thomson relation during solidification. Such a check is particularly important for verifying the absence of solute trapping. In the presence of anisotropy, the Gibbs-Thomson relation can be written as $U_iMc_\infty=-d_0(\hat{n})\kappa-\theta_i$. When applied in the direction of the horizontal dendrite growth axis [4], it becomes

$$U_i=\frac{-d_0(1-15\varepsilon)/\rho-\theta_i}{Mc_\infty}. \tag{76}$$

By recording the dendrite tip radius and interface temperature during the simulations, U_i can be calculated as a function of distance along the dendrite axis and be directly compared to the frozen U profile. The interface temperature θ_i was evaluated at $\phi=0.9$, which can be seen from Fig. 4 to be a reasonable approximation of the temperature of the corresponding sharp interface. Numerical tests indicated that the results are not sensitive to the exact value of ϕ at which θ_i was evaluated. The results of this comparison are shown in Figs. 10(a)–10(d) for the various values of λ. The agreement of the concentrations calculated from Eq. (76) with the predicted solute profile along the dendrite axis is generally excellent. As expected, it deteriorates somewhat with increasing λ.

Figure 11 shows predicted phase field, solute concentration (U), and temperature profiles along the central dendrite axis at a time of $tD/d_0^2=470\,000$. The profiles illustrate the importance of the coupled heat and solute diffusion in the present simulation. The interface temperature is significantly different from the far-field value (-0.55), and temperature variations are present even in the solid. Since $\mathrm{Le}=1$, the solute and temperature boundary layers have approximately the same width.

Since the value of the Lewis number for binary alloys is typically much greater than unity, the growth of a dendrite with $\mathrm{Le}=50$ was also simulated. The other parameters were chosen as $Mc_\infty=0.1$, $\varepsilon=0.02$, $\Delta=0.55$, $k=0.15$, and $\lambda=1.5957$. The equations were solved numerically on a grid of 800×800 nodal points with a grid spacing of $\Delta x/W_0=0.5$ and a time step of $\Delta t/\tau_0=0.001$. Figure 12 shows a snapshot of the dendrite at a time of $tD/d_0^2=3500$. As expected from the large value of Le, the thickness of the thermal boundary layer is much larger than that of the solutal boundary layer. Even though the Lewis number is large, the initial melt concentration is chosen low enough that the interface temperature is significantly different from the far-field value. Some temperature variations are present even in the solid. The dimensionless concentration c/c_∞ is plotted separately for the solid and liquid regions in the left quadrants. A complex microsegregation pattern can be observed in the solid. Regions with high positive curvatures during solidification have high solute concentrations, and vice versa. The liquid inside the deep pockets near the center is virtually homogeneous.

Figure 13 shows the temporal evolution of various dendrite growth parameters for the dendrite of Fig. 12. Note that at about $tD/d_0^2=2400$ a steady growth regime is almost achieved. At later times, the effect of the interaction of the

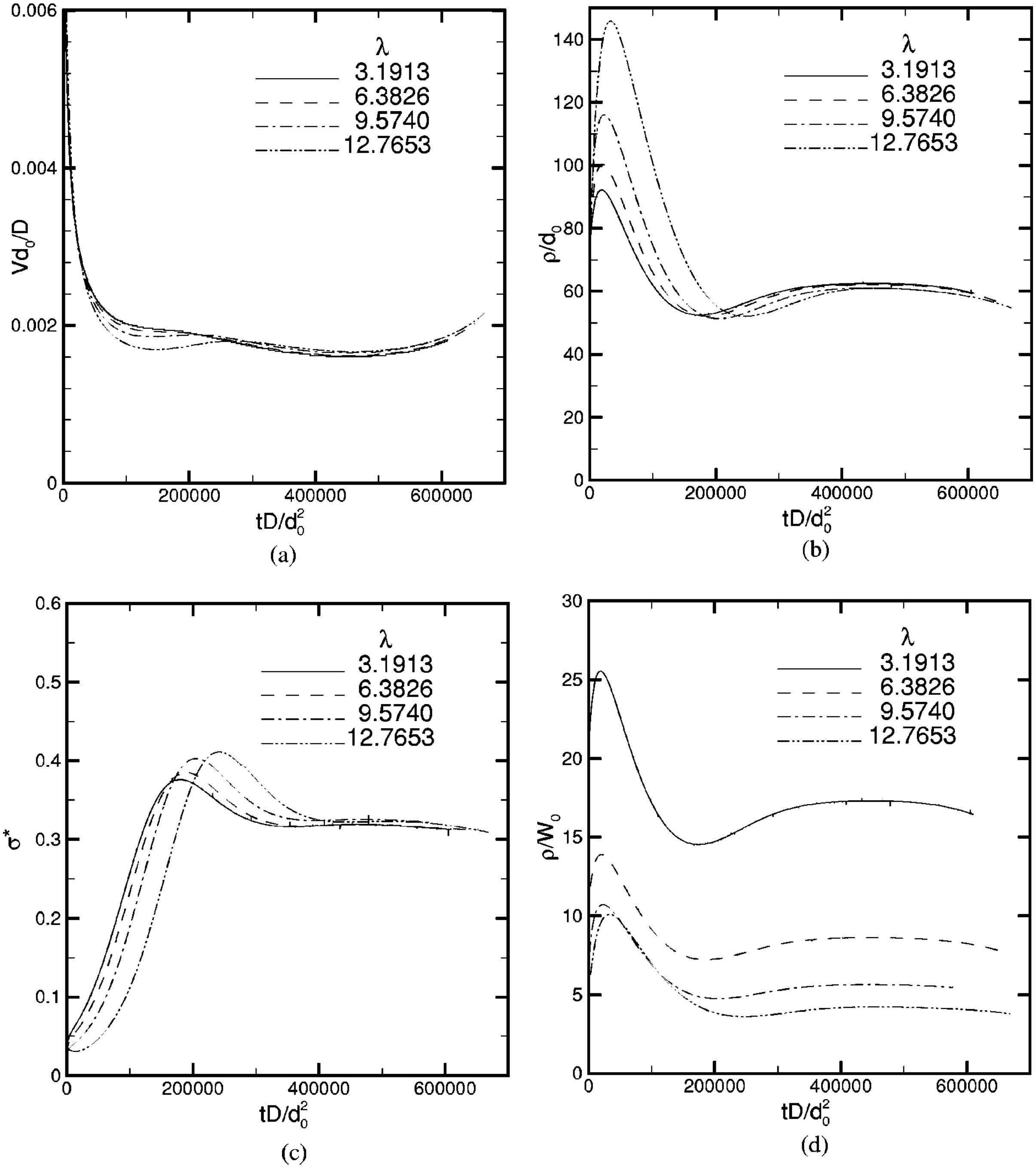

(a) (b)

(c) (d)

FIG. 9. Predicted temporal variation of various growth parameters for two-dimensional dendritic solidification of a binary alloy into an undercooled melt with coupled heat and solute diffusion (Le$=$1, $Mc_\infty$$=$0.5325, $k$$=$0.15, $\varepsilon$$=$0.02, and $\Delta$$=$0.55). The lines in each graph correspond to different λ (i.e., interface width), while keeping the physical domain and initial seed sizes the same.

thermal boundary layer with the domain wall becomes noticeable. Note, however, that the selection parameter $\sigma^* = 2Dd_0/(\rho^2 V)$ appears to remain constant. The ratio ρ/W_0 is approximately equal to 8 after the initial transient, indicating that the results are close to but not fully converged (see Fig. 9). Figure 14 shows a comparison of the predicted U profile in the solid along the dendrite axis with that calculated from the Gibbs-Thomson relation, Eq. (76). In this case, the agreement is not as good as in the Le$=$1 case, but the difference always remains within 5%.

VIII. CONCLUSIONS

We have presented a computationally tractable phase-field model to simulate the solidification of a dilute binary alloy with coupled heat and solute diffusion. The thin-interface analysis of this model makes it possible to carry out simulations using interface widths larger than the capillary length but smaller than the radius of curvature of the interface, as well as for vanishing interface kinetic effects. The antitrapping term in the solute conservation equation effectively

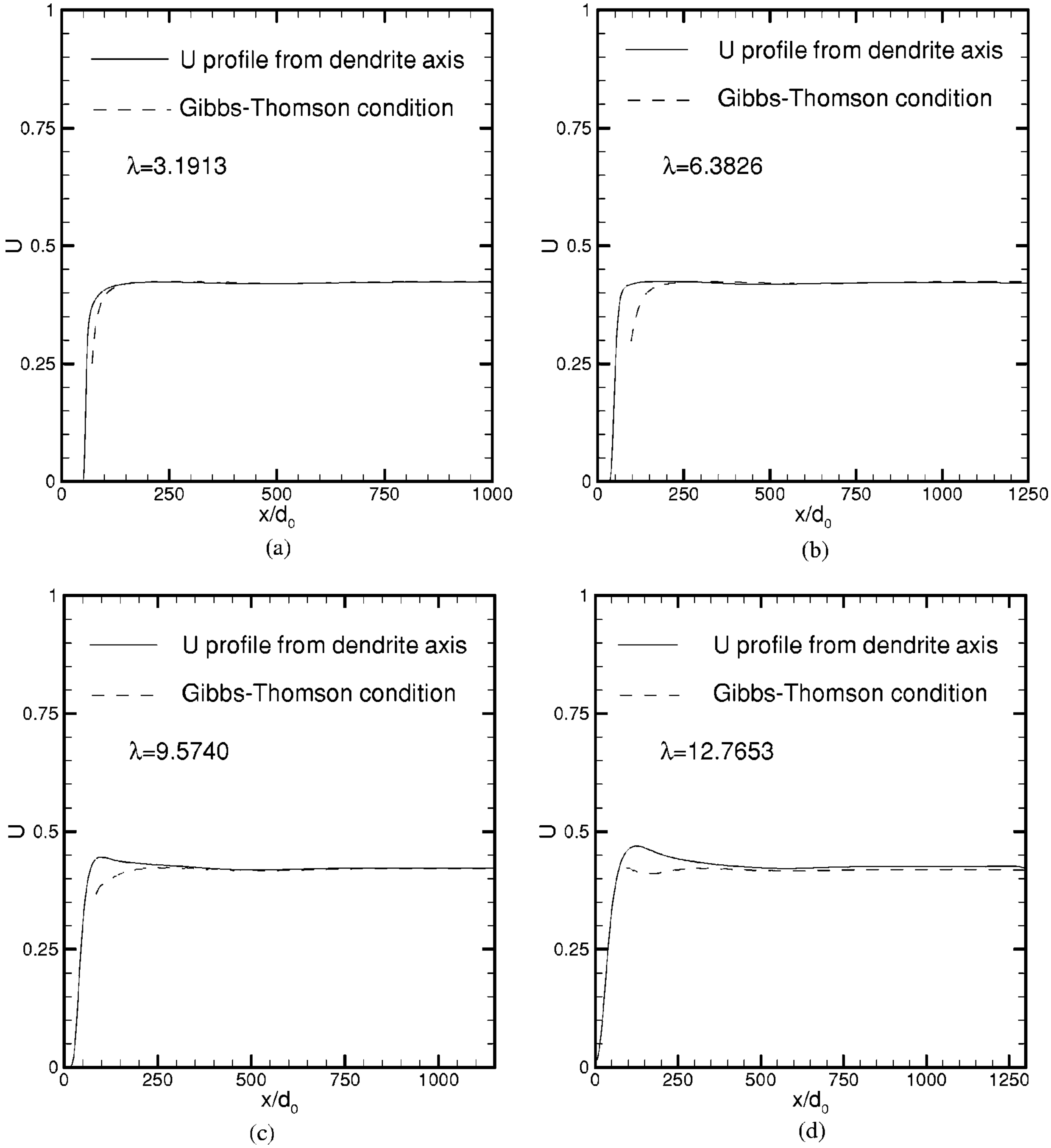

FIG. 10. Comparison of the predicted dimensionless concentration profile in the solid along the central dendrite axis with concentrations in the solid at the interface computed from the Gibbs-Thomson condition, Eq. (76). The simulations correspond to the thermosolutal dendrite of Fig. 9 (Le=1); the four graphs are for different values of λ (i.e., interface width), while keeping the physical domain and initial seed sizes the same.

eliminates the solute trapping effect and other spurious corrections to the mass conservation condition corresponding to interface stretching and surface diffusion [5,14]. In addition, this term makes the model applicable to unequal solutal diffusivities in the solid and liquid.

The model was first validated against an analytical sharp-interface solution for the case of steady one-dimensional solidification of a binary alloy into a hypercooled melt. Convergence of the phase-field results was obtained with decreasing interface Péclet numbers, as expected. Additional validation was presented for the case of isothermal dendritic solidification of a binary alloy in two dimensions by comparing the results to the model of Karma [5]. The full model was then applied to dendritic solidification with coupled heat and solute diffusion. For the case of Le=1, convergence of the results for decreasing values of the coupling parameter λ (i.e, the interface width) was demonstrated. The solute profile in the solid along the dendrite growth axis is in excellent agreement with concentrations calculated from the Gibbs-Thomson relation, indicating that solute trapping is indeed

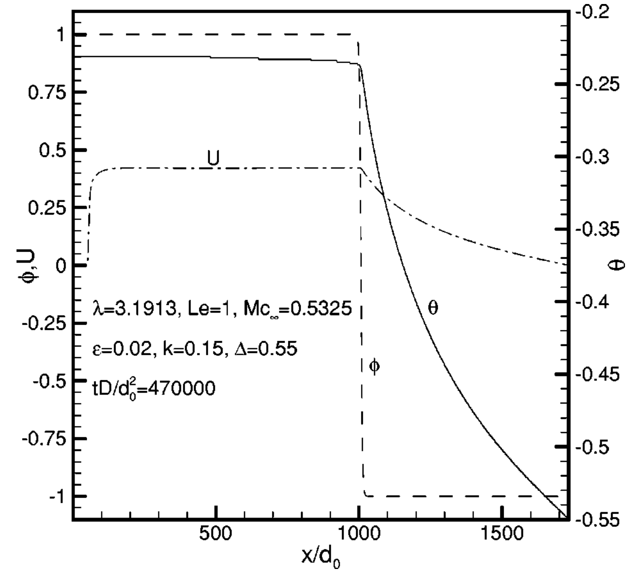

FIG. 11. Predicted phase field U and θ profiles along the central dendrite axis for the thermosolutal dendrite of Fig. 9 (Le=1, λ=3.1913 only) at a time of tD/d_0^2=47 000.

absent. A case where the Lewis number is large (Le=50), but the melt concentration is small enough that the system is nonisothermal, was also simulated. These simulations revealed complex microsegregation patterns and temperature nonuniformities in the solid. Future studies include the application of the present model to examine the operating state of alloy dendrites for small solute concentrations where thermal and solutal effects are both important.

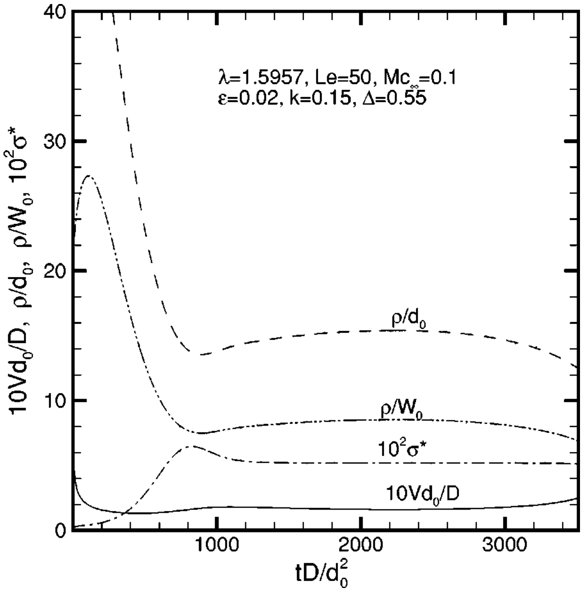

FIG. 13. Predicted temporal evolution of various growth parameters for the thermosolutal dendrite of Fig. 12 (Le=50).

ACKNOWLEDGMENTS

This work was supported by NASA under Contracts Nos. NCC8-199 and NNM04AA18G, and DLR under Contract No. 50WM0035.

APPENDIX

A planar interface moving at velocity V in the $+x$ direction is considered. Defining the dimensionless variable $y=x/W$,

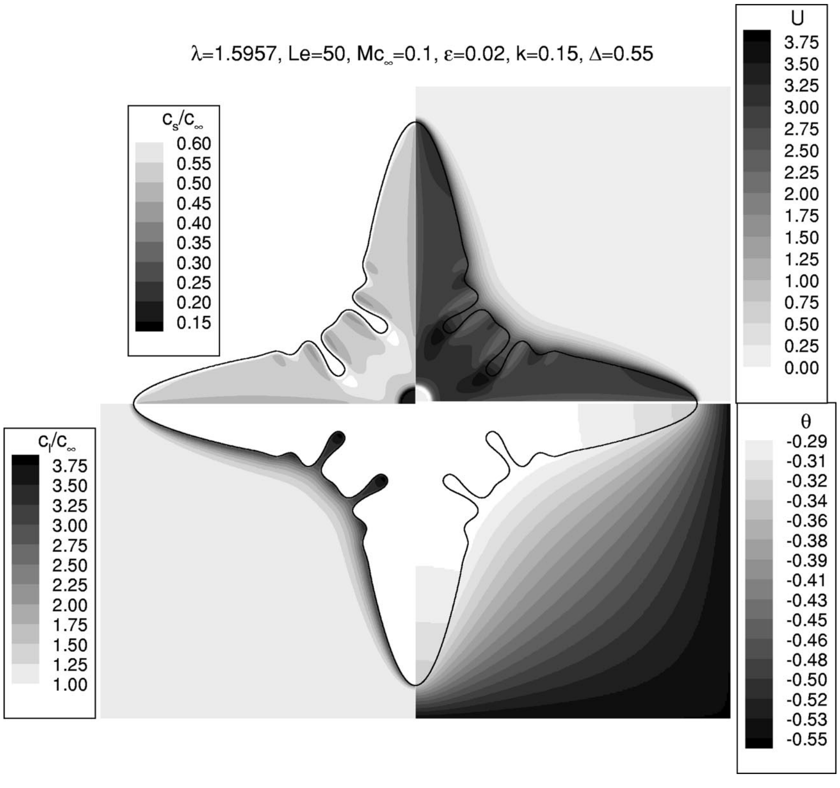

FIG. 12. Predicted results for two-dimensional dendritic solidification of a binary alloy into an undercooled melt with coupled heat and solute diffusion for Le=50 at tD/d_0^2=3500. The upper and lower right quadrants show the dimensionless concentration U and temperature fields, respectively; the left quadrants both show concentration c/c_∞ fields, with different scales used in the upper and lower quadrants in order to better visualize the concentration variations in the solid and liquid, respectively.

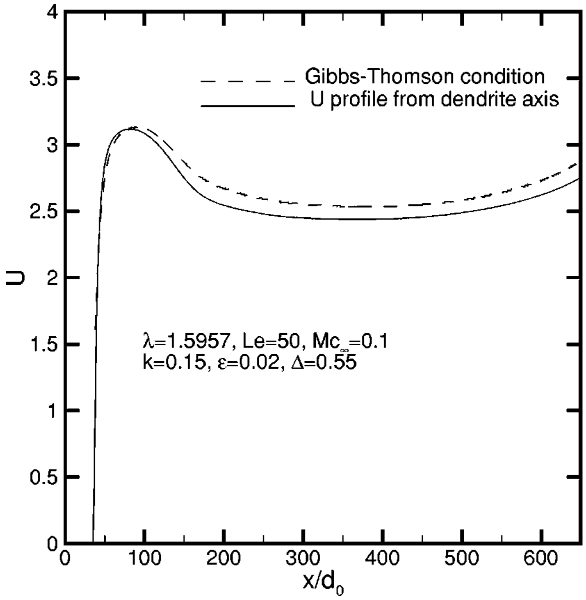

FIG. 14. Comparison of the predicted dimensionless concentration profile in the solid along the central dendrite axis with concentrations in the solid at the interface computed from the Gibbs-Thomson condition, Eq. (76), for the thermosolutal dendrite of Fig. 12 (Le=50).

and rewriting the phase-field equations (45)–(47) in a frame moving with the interface, the set

$$-p\tilde{D}\partial_y\phi = \partial_y^2\phi + \phi - \phi^3 - \lambda g'(\phi)(\theta + Mc_\infty U), \quad \text{(A1)}$$

$$\frac{1-k}{2}\partial_y U = \partial_y\left(\frac{1-\phi}{2}\partial_y U + \frac{p}{2\sqrt{2}}[1+(1-k)U]\partial_y\phi\right) - \frac{p}{2}\partial_y\{\phi[1+(1-k)U]\}, \quad \text{(A2)}$$

$$-p\partial_y\theta = \mathrm{Le}\partial_y^2\theta - \frac{p}{2}\partial_y\theta, \quad \text{(A3)}$$

is obtained, where the interface Péclet number $p = WV/D$ is typically a small parameter in mesoscale simulations. Following the same steps as Karma and Rappel in Sec. III A of Ref. [4], solutions of Eqs. (A1)–(A3) are seeked perturbatively by expanding the solutions in the diffuse interface region (inner solutions) in powers of p:

$$\phi = \phi_0 + p\phi_1 + p^2\phi_1 + \ \dots, \quad \text{(A4)}$$

$$U = U_0 + pU_1 + p^2U_1 + \cdots, \quad \text{(A5)}$$

$$\theta = \theta_0 + p\theta_1 + p^2\theta_1 + \cdots. \quad \text{(A6)}$$

Substituting these expansions into Eqs. (A1) and (A2), yields for solutions at leading order the stationary phase-field profile $\phi_0 = -\tanh[y/(\sqrt{2}W)]$ together with the equilibrium condition $\theta_0 + Mc_\infty U_0 = 0$ that corresponds to a stationary interface, where θ_0 and U_0 are constants. At first order in p, Eqs. (A1) and (A2) yield the system of linear equations

$$[\partial_y^2 + (1 - 3\phi_0^2)]\phi_1 \equiv L\ \phi_1 = \partial_y\phi_0 - \lambda g'(\phi_0)(\theta_1 + Mc_\infty U_1), \quad \text{(A7)}$$

$$\tilde{D}\partial_y[(1-\phi_0)\partial_y U_1] - [1 + (1-k)U_0](\partial_y\phi_0 - \partial_y^2\phi_0/\sqrt{2}) = 0, \quad \text{(A8)}$$

$$\mathrm{Le}\partial_y^2\theta_1 - \tfrac{1}{2}\partial_y\phi_0 = 0. \quad \text{(A9)}$$

Explicit expressions for U_1 and θ_1 can be obtained by integrating twice with respect to y the last two equations and by using the fact that $\partial_y\phi_0 = -(1-\phi_0^2)/\sqrt{2}$. This yields

$$U_1(y) = \overline{U_1} - y + \frac{1 + (1-k)U_0}{2}\int_0^y dy\,\phi_0(y), \quad \text{(A10)}$$

$$\theta_1(y) = \overline{\theta_1} + Ay + \frac{1}{2\mathrm{Le}}\int_0^y dy\,\phi_0(y), \quad \text{(A11)}$$

where the first constant associated with integrating once Eq. (A8) is easily obtained by examining the limit in the solid where the diffusivity vanishes. A crucial feature here is that the same function $\int_0^y dy\,\phi_0(y)$ appears in the expressions for U_1 and θ_1 by virtue of the choice of the antitrapping current that yields the combination $(\partial_y\phi_0 - \partial_y^2\phi_0/\sqrt{2})$ in Eq. (A8), as opposed to $(\partial_y\phi_0)$ without this current. This feature makes the thin-interface limit of the isothermal solidification of a dilute alloy [5] essentially identical to the thin-interface limit for the nonisothermal solidification of a pure melt [4]. The same is true here for the thermosolutal problem because of the additive property that $\theta_1 + Mc_\infty U_1$ has a similar asymptotic behavior on the two sides of the interface as θ_1 alone when $c_\infty \to 0$ or as U_1 for fixed temperature. Namely, the large y asymptotic behavior of the inner $U(\theta)$ solution on the liquid side of the interface is the sum of a gradient term, which represents the normal flux of solute (heat), and a constant $U_i(\theta_i)$ that is equal to the value of the outer diffusion field (i.e., field that appears in the sharp-interface equations) on the liquid side of the interface. Adding the zeroth and first order in p solutions, the constants for the two fields are

$$U_i = U_0 + p\left(\overline{U_1} + \frac{1 + (1-k)U_0}{2}F\right) + \cdots, \quad \text{(A12)}$$

$$\theta_i = \theta_0 + p\left(\overline{\theta_1} + \frac{1}{2\mathrm{Le}}F\right) + \cdots, \quad \text{(A13)}$$

where

$$F = \int_0^{+\infty} dy[\phi_0(y) + 1]. \quad \text{(A14)}$$

These constants are the same on the solid side of the interface owing to the property that ϕ_0 is an odd function of y, and hence that $\int_0^{+\infty} dy[\phi_0(y)+1] = \int_0^{-\infty} dy[\phi_0(y)-1]$ [4]. Thus, both the temperature and the chemical potential are continuous at the interface, as illustrated for the U field in Fig. 15.

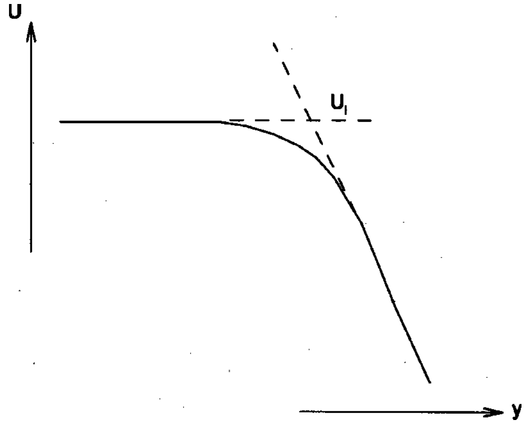

FIG. 15. Schematic plot of U in the diffuse interface region illustrating how U_i is defined.

To complete the derivation, note that β is defined by the relationship $\theta_i + Mc_\infty U_i = -\beta V$. Adding Eq. (A12) multiplied by Mc_∞ to Eq. (A13), and using the equilibrium condition $\theta_0 + Mc_\infty U_0 = 0$ together with the relation $p/V = W/D$, yields

$$\beta = -\frac{W}{D}(\overline{\theta_1} + Mc_\infty \overline{U_1}) - \frac{WF}{2D}\left(\frac{1}{\mathrm{Le}} + Mc_\infty[1 + (1-k)U_0]\right). \tag{A15}$$

The combination $\overline{\theta_1} + Mc_\infty \overline{U_1}$ is now obtained from the condition that Eq. (A7) must have a physically admissible solution. Since $\partial_y \phi_0$ is a homogeneous solution of $\mathcal{L}\partial_y\phi_0$ and $\mathcal{L}$ is a self-adjoint linear operator, the left-hand side of Eq. (A7) must be orthogonal to $\partial_y\phi_0$ for a solution ϕ_1 to exist. This yields the solvability condition

$$\int_{-\infty}^{+\infty} dy\, \partial_y\phi_0 \{\tilde{D}\partial_y\phi_0 - \lambda g'(\phi)[\theta_1(y) + Mc_\infty U_1(y)]\} = 0. \tag{A16}$$

Substituting the earlier expressions for $\theta_1(y)$ and $U_1(y)$ in the above relation, and noting that the terms linear in y give zero contributions because $\partial_y\phi_0$ is an even function of y, the final expression,

$$\beta = \frac{I}{J}\frac{\tau}{W\lambda} - \frac{W(K+JF)}{2DJ}\left(\frac{1}{\mathrm{Le}} + Mc_\infty[1 + (1-k)U_0]\right), \tag{A17}$$

is obtained, where the same integrals as in Sec. 3A of Ref. [4] have been defined:

$$I = \int_{-\infty}^{+\infty} dy (\partial_y\phi_0)^2, \tag{A18}$$

$$J = -\int_{-\infty}^{+\infty} dy\, \partial_y\phi_0 g'(\phi_0), \tag{A19}$$

$$K = \int_{-\infty}^{+\infty} dy\, \partial_y\phi_0 g'(\phi_0) \int_0^y dy'\, \phi_0. \tag{A20}$$

It is now simple to check that β defined by Eq. (A17) is identical to β defined earlier by Eq. (51) with the additional definitions

$$a_1 = \frac{I}{J}, \tag{A21}$$

$$a_2 = \frac{K+JF}{2I}. \tag{A22}$$

---

[1] A. Karma, in *Encyclopedia of Materials: Science and Technology*, edited by K. H. J. Buschow *et al.* (Elsevier, Oxford, 2001), Vol. 7, p. 6873.
[2] W. J. Boettinger, C. Beckermann, A. Karma, and J. A. Warren, Annu. Rev. Mater. Sci. **32**, 163 (2002).
[3] A. Karma and W.-J. Rappel, Phys. Rev. E **53**, R3017 (1996).
[4] A. Karma and W.-J. Rappel, Phys. Rev. E **57**, 4323 (1998).
[5] A. Karma, Phys. Rev. Lett. **87**, 115701 (2001).
[6] J. Tiaden, B. Nestler, H.-J. Diepers, and I. Steinbach, Physica D **115**, 73 (1998).
[7] S. G. Kim, W. T. Kim, and T. Suzuki, Phys. Rev. E **60**, 7186 (1999).
[8] C. Beckermann *et al.*, J. Comput. Phys. **154**, 468 (1999).
[9] J. A. Warren and W. J. Boettinger, Acta Metall. Mater. **43**, 689 (1995).
[10] I. Loginova, G. Amberg, and J. Agren, Acta Mater. **49**, 573 (2001).
[11] C. W. Lan, Y. C. Chan, and C. J. Shih, Acta Mater. **51**, 1857 (2003).
[12] M. J. Aziz, Metall. Mater. Trans. A **27**, 671 (1996).
[13] N. A. Ahmad, A. A. Wheeler, W. J. Boettinger, and J. A. Warren, Phys. Rev. E **58**, 3436 (1998).
[14] B. Echebarria, R. Folch, A. Karma, and M. Plapp (unpublished).
[15] R. F. Almgren, SIAM (Soc. Ind. Appl. Math.) J. Appl. Math. **59**, 2086 (1999).
[16] D. A. Goodman, J. W. Cahn, and L. H. Bennet, Bull. Alloy Phase Diagrams **2**, 29 (1981).